

# Chapter 14

## Kinetic Energy Spectra and Model Filters

William C. Skamarock

**Abstract** We wish to maximize efficiency (accuracy/cost) in the design of atmospheric fluid-flow solvers. An important measure of accuracy for weather and climate applications is a model's ability to resolve meteorologically important features at scales approaching the grid-scale. Simulated kinetic energy spectra provide a useful diagnostic for quantifying a model's resolving capability. Using kinetic energy spectra we illustrate some of the issues affecting the resolution capabilities of models arising from the choice of spatial grid staggering, integration schemes and their implicit filters, and explicit filters. In both Eulerian and semi-Lagrangian formulations, C-grid staggering provides the best resolution of divergent modes that are an important part the KE spectrum in the mesoscale which the global models are now beginning to resolve. Other grid staggarings require special filtering that compromise resolution capabilities. The popular semi-Lagrangian semi-implicit formulations are shown to significantly damp resolvable high-frequency modes and adversely affect their resolving capabilities. While less costly at a given grid density, the SLSI models may well be significantly less efficient than Eulerian models.

### 14.1 Introduction

Clouds and precipitation are among the most important and challenging phenomena that must be accurately treated for climate and Numerical Weather Prediction (NWP) applications. In our existing operational global climate and weather models, clouds and precipitation processes are parameterized, i.e. they are modeled, as opposed to being explicitly represented in the discrete atmospheric fluid-flow

---

W.C. Skamarock

National Center for Atmospheric Research, Boulder, Colorado, USA

e-mail: [skamaroc@ucar.edu](mailto:skamaroc@ucar.edu)

The National Center for Atmospheric Research is supported by the National Science Foundation.

solvers. The need to resolve clouds and cloud systems, and the availability of more powerful computers, are driving us to apply global atmospheric models at increasingly higher spatial and temporal resolutions. In the research setting, the coming introduction of peta-scale computers will permit us to regularly produce global simulations using horizontal grid spacing of a few kilometers for weather and short-term climate (seasonal) applications. At this grid spacing we remove the deep convective parameterizations that are seen as most problematic, but we are left with the problem of modeling sub-grid entrainment and detrainment in these poorly-resolved clouds (Tao and Moncrieff 2009; Weisman et al. 1997; Bryan et al. 2003). The denser grids will also permit better resolution of topography, land use, land-sea boundaries, and other atmospheric forcing mechanisms as well as provide better resolution of flow dynamics not related to clouds, such as land-sea breezes, fronts, and mountain waves.

When solving the Navier–Stokes equations for atmospheric fluid flow, we increase resolution because we wish to better resolve features that are marginally resolved at current resolutions, and because we wish to explicitly simulate, or resolve, flow phenomena that were absent or parameterized in the less-well-resolved solutions. The former reason is related to the classical numerical analysis understanding regarding the numerical solution of Partial Differential Equations (PDEs) – increasing resolution will lower solution error, with infinite resolution producing a perfect solution. It must be understood, however, that atmospheric flow solutions do not converge in the strict sense. New phenomena appear, and we ultimately strive only for statistical convergence. The explicit simulation of new flow phenomena and forcings is the critical reason to increase resolution in present-day global climate and NWP models. Global model resolutions are now increasing to a level where mesoscale features begin to be resolved (e.g., the larger-scale aspects of convective cloud systems such as hurricanes, etc.), and we are beginning to resolve phenomena that differ dynamically in a fundamental way from that of planetary- and synoptic-scale flows.

The change in dynamical regimes associated with the newly-resolved phenomena, and the lack of strict solution convergence, raise a number of questions concerning global solver design and evaluation. Our primary objective in designing atmospheric flow solvers is to maximize efficiency, that is, we wish to attain a given level of accuracy for the smallest computational cost, or we wish to achieve the highest accuracy for a given cost. In this paper we consider how observations and model simulations of the atmospheric kinetic energy spectra can be used to quantify solution accuracy, thus allowing us to examine solver characteristics involving spatial and temporal discretizations and model filtering, and ultimately model efficiency. Some aspects of existing global models, such as the time integration and spatial interpolation schemes used in semi-Lagrangian models, the choice of horizontal grid staggering, and filter choices used in some large-scale global models, will be shown to adversely affect solver performance for mesoscale and cloudscale phenomena.

## 14.2 Kinetic Energy Spectra and Atmospheric Dynamics

Nastrom and Gage (1985) used aircraft observations of winds from the Global Atmospheric Sampling Program (GASP) to compute kinetic energy (KE) spectra for horizontal length scales from a few kilometers to several thousand kilometers. Lindborg (1999) similarly used aircraft observations from the Measurement of ozone and water vapor by Airbus in-service aircraft (MOZAIC) program to compute structure functions and a kinetic energy spectrum. Results from both studies, depicted in Fig. 14.1, illustrate the characteristic behavior of the kinetic energy spectrum. At larger scales (horizontal wavelengths greater than approximately several hundred kilometers) the spectrum scales as  $k^{-3}$  where  $k$  is the horizontal wavenumber. For shorter wavelengths (higher wavenumbers) the spectrum scales as  $k^{-5/3}$ , and a small transition region exists between the two regimes. While it is widely accepted that the dynamics of the  $k^{-3}$  regime correspond to a downscale cascade of enstrophy, there is no consensus concerning the  $k^{-5/3}$  regime (Lilly et al. 1998; Lindborg 2006). The characterization of the  $k^{-5/3}$  regime represents one of the major unanswered questions in mesoscale atmospheric dynamics.

The KE spectrum can also be computed from model simulations. This spectrum from a high-resolution simulation using the Advanced Research Weather Research and Forecast model (ARW, Skamarock and Klemp 2008; Skamarock et al. 2008) is shown in Fig. 14.2, and this simulated spectrum reproduces the transition. This behavior has also been found in simulations from other models (Lilly et al. 1998; Lindborg and Berthouwer 2007; Hamilton et al. 2008) and, while there are variations in the spectra as a function of pressure, geographical region and weather regime (Skamarock 2004), the transition is always apparent.

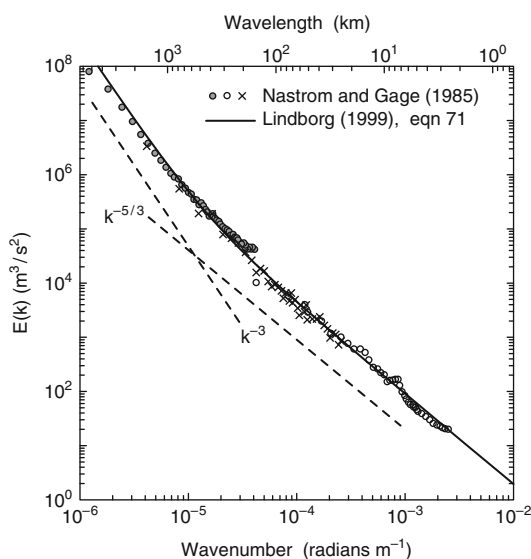
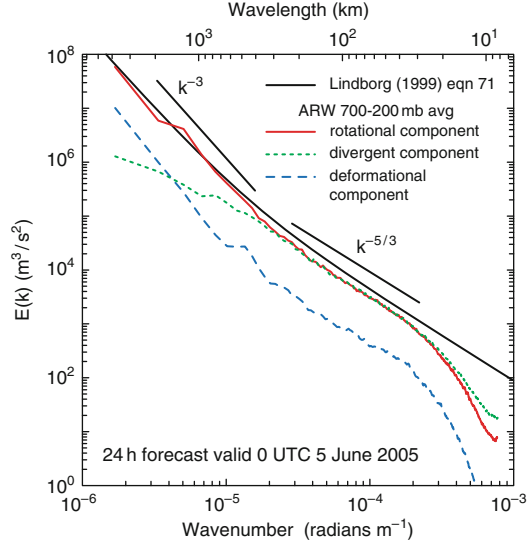


**Fig. 14.1** Nastrom and Gage (1985) spectrum derived from the GASP aircraft observations (symbols) and the Lindborg (1999) functional fit to the MOZAIC aircraft observations. The figure is from Skamarock (2004)

**Fig. 14.2** Decomposed kinetic energy spectra for a spring-season forecast over the continental U.S. The forecasts were produced using the ARW with  $\Delta x = 4$  km. The figure is from Skamarock and Klemp (2008)



The simulated spectrum can be decomposed into a rotational component  $V_\psi$ , a divergent component  $V_\chi$ , and a deformational component  $V_{def}$ , where  $V = V_\psi + V_\chi + V_{def}$  and the velocities are given as

$$V_\psi = k \times \nabla \psi$$

$$V_\chi = \nabla \chi$$

$$V_{def} = V - V_\psi - V_\chi.$$

$\psi$  and  $\chi$  are defined as

$$\nabla^2 \psi = \zeta, \quad \zeta = k \cdot \nabla \times V$$

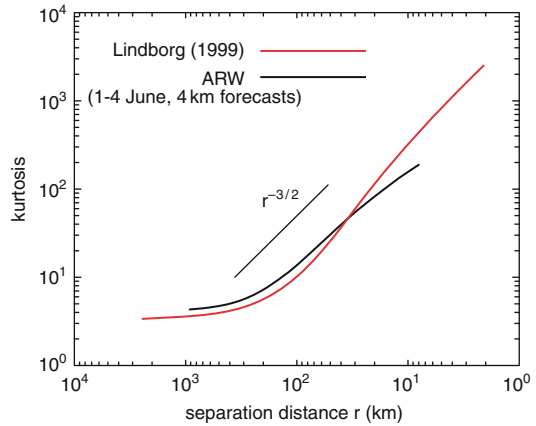
$$\nabla^2 \chi = D, \quad D = \nabla \cdot V,$$

where  $k$  is the unit vector normal to the horizontal coordinate surface. The deformational component arises from the presence of lateral boundaries and would be absent in a decomposition of the wind fields over the globe. At large scales the kinetic energy is dominated by rotational energy, and the transition to the  $k^{-5/3}$  regime occurs when the energy in the divergent component becomes comparable to that in the rotational component (see Fig. 14.2). Lindborg (2007) argues that it can also be deduced from the aircraft observations. Thus the atmospheric dynamics are seen to be changing in a fundamental way as one moves from large scale to the mesoscale, and one important aspect of this change is the importance of divergent motions to the mesoscale KE spectrum.

Lindborg (1999) also presents results for the kurtosis which is defined as

$$\text{kurtosis: } \frac{\langle \delta u^4 \rangle}{\langle \delta u^2 \rangle^2},$$

**Fig. 14.3** Kurtosis computed using observations from MOZAIC (Lindborg 1999) and from spring forecasts for 1–3 June 2003 over the continental U.S. using the ARW model with  $\Delta x = 4$  km (Done et al. 2004)



where  $\delta u = u(x + r) - u(x)$  for a distance  $r$  along an aircraft track, and  $u$  is the along-track velocity. Figure 14.3 shows a plot of the kurtosis computed from the MOZAIC observations and from ARW simulations. For large-scale flow, where the velocity field is observed to possess a Gaussian probability density function (PDF), the kurtosis should equal 3 (Lindborg 1999; Frisch 1995), as is found in the plot. In the mesoscale region the kurtosis increases dramatically and scales as approximately  $r^{-3/2}$ , indicating that there is significant intermittency at small scales. Both observations and model results exhibit this strong intermittency at the mesoscale and cloudscale where significant energy is in the horizontally divergent component of the flow.

The changes in atmospheric dynamics indicated in the spectrum and the kurtosis have several implications for solver design. The mesoscale and cloud-scale motions that higher-resolution models resolve represent motions that are entirely parameterized in large-scale models. Examples of the parameterizations include those for convection and gravity-wave propagation and breaking (gravity-wave drag). These parameterizations are problematic and are a major impetus for moving to higher resolution where the parameterizations can be removed. Toward this end, the solvers must be able to accurately simulate horizontally divergent motions, which has not been a priority in existing large-scale models. In the following sections we examine some of the issues involved in solver design and ability to accurately simulate divergent motions.

### 14.3 Model Dissipation and Spectral Damping

In the  $k^{-3}$  spectral regime there is a downscale cascade of enstrophy, whereas the  $k^{-5/3}$  there appears to be a net downscale cascade of energy (e.g., Lindborg and Cho, 2000). In either case, enstrophy or energy must be removed as it cascades to the highest wavenumbers represented in the model discretization. Failure to provide

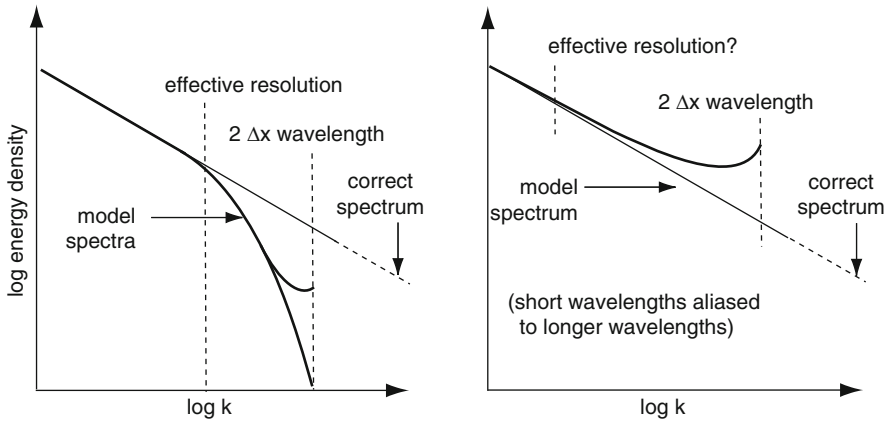


**Fig. 14.4** Schematic depicting the possible behavior of spectral tails derived from model forecasts. Using the methodology outlined in the Appendix to compute the spectra, limited area models (including ARW) usually produce the slightly upturned tail shown in the *left panel*. Adapted from Skamarock (2004)

sinks for these cascades results in an unphysical buildup of energy or enstrophy at the smallest scales. In addition, most numerical methods do not accurately simulate these high wavenumber modes, and it is beneficial to remove the energy in these modes so that energy is not erroneously aliased onto the smaller wavenumber (well-resolved) modes. The energy density should drop considerably in the simulated spectrum in the highest wavenumbers as a result of this filtering; this is depicted schematically in Fig. 14.4 and it is apparent in the simulated spectrum in Fig. 14.2. We define the *effective resolution* of a solver as the point at which the slope of the simulated spectrum becomes greater than the slope of the expected (or observed) spectrum, as is indicated in Fig. 14.4. In designing a solver and dissipation mechanisms we wish to maximize the effective resolution (i.e. have an effective resolution at the highest wavenumber possible) while removing energy from the highest wavenumbers thereby minimizing aliasing. In principle, higher-order methods allow a higher effective resolution if they are combined with appropriate energy and enstrophy sinks.

There are many approaches to providing the necessary enstrophy and energy sinks in the solvers (Chap. 13). Many models use explicitly computed horizontal mixing terms of the form

$$\frac{\partial \phi}{\partial t} = \dots (-1)^{(n+2)/2} \nu_n \frac{\partial^n \phi}{\partial x_i^n} \quad (14.1)$$

where  $n$  is an even integer and  $\nu_n$  is referred to as an eddy viscosity when  $n = 2$  or a hyperviscosity when  $n > 2$ . Higher values of  $n$  produce filters that are more scale selective (the damping rate as a function of wavenumber drops off more quickly). There is no physical justification for (14.1) for large-scale and mesoscale flows. For

atmospheric Large Eddy Simulation (LES) resolutions ( $\Delta x < 100$  m), theory exists for defining the eddy viscosity  $\nu_2$  (Mason 1994; Wyngaard 2004).

A second mechanism for dissipating energy, specifically targeting energy in the divergent motions, is horizontal divergence damping. This filter is usually implemented in the form of a damping term in the horizontal momentum equations:

$$\frac{\partial u_i}{\partial t} = \dots + \nu_d \frac{\partial}{\partial x_i} (\nabla_h \cdot \mathbf{V}), \quad (14.2)$$

where  $\mathbf{V}$  is the horizontal velocity.

That this damping targets horizontally divergent motions can be seen by taking the horizontal divergence of the momentum equations (14.2) which results in

$$\frac{\partial}{\partial t} (\nabla_h \cdot \mathbf{V}) = \dots + \nabla_h^2 (\nabla_h \cdot \mathbf{V}).$$

Horizontal divergence damping has been used in many large-scale models to filter gravity waves, especially those that resulted from imbalances in real-data initializations (Dey 1978; Janjic 1990). There are models today still using this formulation, including the Finite Volume (FV) core in the Community Climate System Model (CCSM) (Collins et al. 2004) and the Nonhydrostatic Mesoscale Model (NMM) used operationally for limited area NWP at the National Centers for Environmental Prediction (NCEP) (Janjic 2003). Horizontal divergence damping can also be extended to higher order ( $n > 2$ ):

$$\frac{\partial u_i}{\partial t} = \dots + (-1)^{(n+2)/2} \nu_d \frac{\partial^{(n-1)}}{\partial x_i^{(n-1)}} (\nabla_h \cdot \mathbf{V}),$$

or alternatively as in the FV core ( $n = 4$ ; Peter Lauritzen, personal communication)

$$\frac{\partial u_i}{\partial t} = \dots + (-1)^{(n+2)/2} \nu_d \frac{\partial}{\partial x_i} \nabla_h^{n-2} (\nabla_h \cdot \mathbf{V}).$$

Horizontal divergence damping can have a significant impact on a model's ability to produce the  $k^{-5/3}$  KE spectra as demonstrated in Skamarock (2004). Given that the KE in the  $k^{-5/3}$  region is composed of both rotational and divergent energy, horizontal divergence damping cannot be the sole energy sink employed in a model formulation. Furthermore, convection and convective transport are strongly divergent motions, thus horizontal divergence damping preferentially filters them. Since these processes are becoming increasingly important as we employ higher resolution grids, preferentially damping these modes is counter to our objectives, and no mesoscale or cloudscale resolving models use this form of damping aside from the nonhydrostatic FV core (William Putnam, personal communication) and the NCEP NMM (Janjic 2003). While there may be some computational aspects of model formulations for which the use of horizontal divergence damping may appear

beneficial, these problems can be avoided in the model formulation directly or by using other less-deleterious filters.

Another class of filters in numerical models are those that are implicit in the numerical discretization. The filters may damp temporally because the damping is implicit in the time integration, the damping may be part of the transport algorithm or spatial interpolation scheme that is part of the spatial discretization, or it may be intertwined in both the spatial and temporal schemes. These schemes can affect a model's ability to resolve divergent motions and the mesoscale portion of the spectra.

## 14.4 Grid Staggering and Spatial Discretizations

One dynamical description of the mesoscale is that scale in which the kinetic energy of the horizontally divergent motions approaches the same order as that of the rotational motions, and this occurs where the KE spectrum assumes a  $k^{-5/3}$  behavior. Given the critical role of horizontally divergent motions in the mesoscale, it is important to consider how discretizations resolve these motions. One important factor influencing the numerical discretization is the staggering of the variables in the model grid (Chap. 3). Figure 14.5 depicts three different horizontal grid staggarings (commonly referred to as the A, C, and D grids – see [Arakawa and Lamb \(1977\)](#)) used in global and some limited-area mesoscale models.

Consider the simple second-order finite differencing of the height (pressure) gradient, divergence and Coriolis terms for the vector momentum form of the shallow-water equations that is commonly used on these grids.

A grid	C grid	D grid
$h_x \sim \delta_{2\Delta x} h$	$h_x \sim \delta_{\Delta x} h$	$h_x \sim \delta_{2\Delta x} \bar{h}^y$
$u_x \sim \delta_{2\Delta x} u$	$u_x \sim \delta_{\Delta x} u$	$u_x \sim \delta_{2\Delta x} \bar{u}^y$
$fv \sim f v$	$fv \sim f \bar{v}^x{}^y$	$fv \sim f \bar{v}^x{}^y$

where the discrete operators

$$\delta_{\Delta x} \phi = (\phi_{x+\Delta x/2} - \phi_{x-\Delta x/2}) / \Delta x$$

$$\bar{\phi}^y = (\phi_{y+\Delta y/2} + \phi_{y-\Delta y/2}) / 2.$$

[Randall \(1994\)](#) presents a linear analysis of the response of the second-order centered spatial approximations for the linearized shallow water equations (inertia-gravity waves) discretized on these grids using the vector-momentum form of the equations (he also examines the Z-grid discretization that use a vorticity-divergence formulation of the shallow-water equations).

Consider the response for rotationally dominated waves. The A grid response is superior to the response of the C and D grids (see [Randall 1994](#), Fig. 2,  $\lambda/d = 0.1$ ;



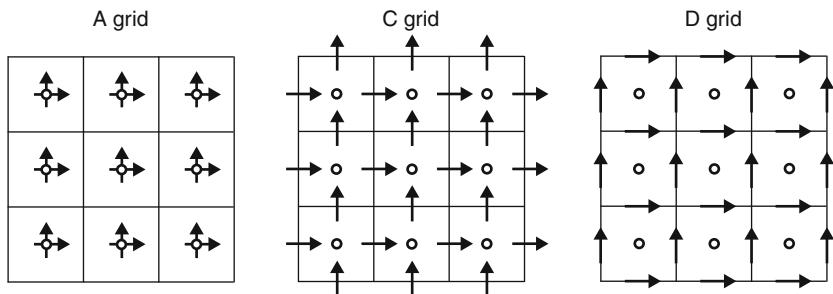


Fig. 14.5 Schematic depicting the Arakawa A, C and D grids

the D-grid response, not shown, is essentially that of the C grid). The superiority of the A grid is especially pronounced in the upper half of the wave spectrum, where the C and D grid frequencies are zero for the  $2\Delta x$  and  $2\Delta y$  modes. The erroneous zero frequency is a result of the averaging needed for interpolating the tangential velocity ( $\overline{v}^{xy}$ ) on these two grids, whereas the A grid needs no averaging for the Coriolis term. The zero frequency for the  $2\Delta$  modes on the C and D grids means that the modes are stationary and the grid does not *see* them, and this is referred to as a *null space* in the solution. The poorer response for inertial waves is the primary reason why few large-scale models use the C or D grids.

The frequency response for waves dominated by horizontal divergence (gravity waves) on these grids is given in Randall's figure 1. Here the C grid response is superior to both the A and D grids, and the A and D grids both have erroneous zero-frequencies for the  $2\Delta$  modes. The averaging needed on both the A and D grids is responsible for these zero frequencies, and as a result the A and D grids do not *see* these  $2\Delta$  modes. Most meso- and cloud-scale models use the C grid because of its superior gravity-wave response, although some modelers use the A grid because it can be advantageous to have all variables defined in the cell center for some discretizations of transport.

To deal with grid-scale modes that have zero frequency, filters must be used to remove the energy in these modes if energy accumulates there. The inertial waves have, however, little energy at scales below the Rossby radius, and for horizontal grid-spacing of  $O(100 \text{ km})$  or less, models using the C grid do not appear to have problems with the zero-frequency  $2\Delta$  inertial mode. For the gravity-wave modes, at meso- and cloud-scale resolutions there is a downscale cascade of energy that will result in energy accumulating in the  $2\Delta$  modes. Filters will be needed on all grids to remove this energy.

To illustrate some of these effects, Fig. 14.6 presents KE spectra computed in the lower stratosphere from aquaplanet simulations for two different CCSM cores – the spectral Eulerian core and the Finite Volume (FV) core (Collins et al. 2004). The KE spectra are decomposed into rotational and divergent components. There is a suggestion of a transition from the large-scale  $k^{-3}$  character to a shallower slope occurring around spherical wavenumber 100 in the spectral Eulerian core spectrum, and this

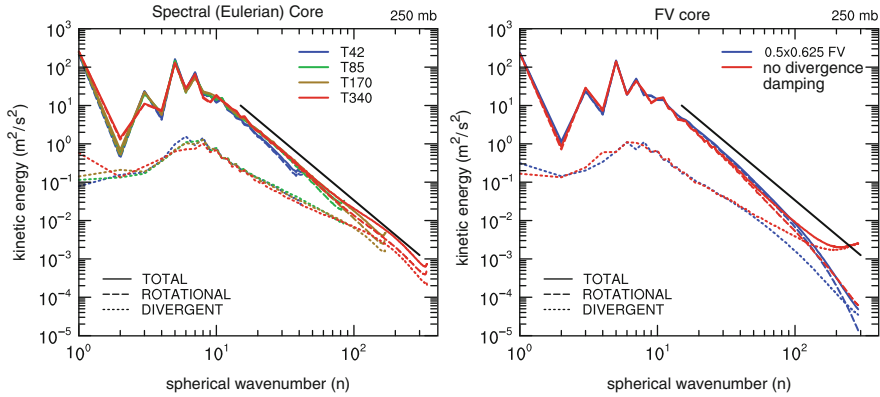


**Fig. 14.6** Kinetic energy (*solid lines*) as a function of spherical wavenumber for the CCSM spectral (Eulerian, *left*) core and the CCSM FV core (*right*) derived from aquaplanet simulations. The total KE is broken into divergent and rotational components (*dashed lines*) for both *cores* and the *solid black lines* shows the  $k^{-3}$  slope. The figures are courtesy of David Williamson

is where the energy in the divergent modes, that behaves as  $k^{-5/3}$ , becomes similar to the rotational mode energy. This behavior is similar to that exhibited by the ARW spectrum (Fig. 14.2) and spectra from other global models (Takahashi et al. 2006), and we would expect that the transition would be better resolved with increasing horizontal resolution. While the spectrum for the spectral Eulerian core does not drop off as rapidly as the ARW spectrum (Fig. 14.2) at the highest wavenumbers, the filters in the model are removing energy as evidenced in the increasing slope beginning around spherical wavenumber 200 in the T340 spectrum.

Two spectra are plotted for the FV dynamical core (Fig. 14.6, *right panel*), one from the standard configuration and a second from a simulation with no horizontal divergence damping. The spectrum from the standard configuration of the FV core depicts a spectral slope that is increasing beyond  $k^{-3}$  starting around  $15\text{--}20 \Delta x$ . This evidence of strong filtering appears in both the rotational energy and the divergent energy. There are two numerical filters in the FV core – the monotonicity constraint in the PPM-based advection and interpolation scheme (Lin and Rood 1997), and the horizontal divergence damping. The filtering provided by the horizontal divergence damping is illustrated by comparing the standard-configuration spectrum with that produced with the horizontal divergence damping turned off. There is only a small difference in the rotational component of the spectrum but there is a major buildup of energy at the highest wavenumbers in the divergent component of the spectrum when divergence damping is not used. As discussed in the previous section, the D-grid formulation of the FV core does not see the  $2\Delta x$  divergent modes. Special filters (horizontal divergence damping in this case) must be used to remove energy for this null space on the grid. C-grid models used in meso- and cloud-scale applications (e.g., ARW Skamarock and Klemp 2008, Coupled Ocean-Atmosphere Prediction System (COAMPS) (Hodur 1997), Advanced Regional Prediction System (ARPS, Xue et al. 1990) and global

models using the C-grid discretization (e.g., United Kingdom Meteorological Office (UKMO) model (Staniforth and Wood 2008), global ARW (Skamarock et al. 2008) do not need and do not use these filters, and generally exhibit a much higher effective resolution (typically between 6 and 10  $\Delta x$ ) than evidenced by the FV core spectrum in Fig. 14.6 (15–20  $\Delta x$ ).

## 14.5 Semi-Implicit Semi-Lagrangian Formulations

Many operational global NWP and climate modeling centers are using semi-implicit formulations in conjunction with semi-Lagrangian dynamics (e.g., UKMO/Hadley Center, Staniforth and Wood 2008; Canadian Meteorological Centre (CMC) Meteorological Research Branch (MRB) Global Environmental Multiscale (GEMS) model, Yeh et al. 2002; European Center for Medium Range Forecasting (ECMWF 2006). These semi-Lagrangian semi-implicit (SLSI) formulations allow for long timesteps because the semi-implicit portion of the formulation removes the timestep restriction associated with propagating gravity (and acoustic) waves while the semi-Lagrangian portion of the scheme largely removes the timestep restriction due to advection. Typically, SLSI models run with timesteps five to ten times that of their Eulerian counterparts. The SLSI cost per timestep is significantly greater than Eulerian models because of the need to compute trajectories and interpolate variables to the departure points, and because of the need to perform a global inversion in the implicit formulation, but this increased cost is offset by using the larger timestep.

The filtering characteristics of SLSI schemes have not been closely examined for meso- and cloud-scale applications. In Shutts (2005), it is shown that the KE spectrum of the ECMWF model does not transition to the  $k^{-5/3}$  mesoscale behavior for resolutions where a transition should be resolved. Shutts introduces a backscatter forcing into the system to put energy into these scales, but he does not speculate on why the system does not predict the transition. Palmer (2005, personal communication) found that reducing the timestep in the SLSI model to values used in similarly configured Eulerian models (in this case 1/5 of the SLSI timestep) did not change the KE spectrum – a transition to  $k^{-5/3}$  was not observed. Generally, Eulerian models do predict this transition at these resolutions. In this section we examine dissipation mechanisms in SLSI numerics to see if they may be responsible for preferentially damping mesoscale motions.

For the SLSI formulation, consider the linearized 1D shallow water equations with variables  $U = U + u(x, t)$  and  $H = H + h(x, t)$ :

$$\frac{du}{dt} + g \frac{\partial h}{\partial x} = 0,$$

$$\frac{dh}{dt} + H \frac{\partial u}{\partial x} = 0.$$

where  $g$  is gravity. The SLSI discretization of these equations can be expressed as

$$u^{t+\Delta t} = \left( u - \frac{1-\epsilon}{2} \Delta t g \delta_x h \right) \Big|_d^t - \left( \frac{1+\epsilon}{2} \Delta t g \delta_x h \right) \Big|^{t+\Delta t}$$

$$h^{t+\Delta t} = \left( h - \frac{1-\epsilon}{2} \Delta t H \delta_x u \right) \Big|_d^t - \left( \frac{1+\epsilon}{2} \Delta t H \delta_x u \right) \Big|^{t+\Delta t},$$

where  $d$  refers to the departure point of the trajectory and  $\epsilon$  is the off-centering parameter for the implicit time integration scheme. Gravel et al. (1993) performed an analysis of this scheme and derived the following amplification factor<sup>1</sup>:

$$\frac{E}{\rho} = \frac{1 - \gamma_3(1 - \epsilon^2) \pm 2i\gamma_3^{1/2}}{1 + \gamma_3(1 + \epsilon)^2} \quad (14.3)$$

where  $E$  is the amplification factor,  $\rho$  is the response function for the semi-Lagrangian advection, and  $\gamma_3 = gH(k\Delta t)^2/4$  where  $k$  is the horizontal wavenumber. It is easily shown that for  $|\rho| \leq 1$  and  $0 \leq \epsilon \leq 1$  the SLSI scheme is absolutely stable. In most models using the full nonlinear implementation for NWP and climate applications,  $0.1 \leq \epsilon \leq 0.2$  is needed for stability. The ECMWF model is run with  $\epsilon = 0$  and filtering needed for the two-time-level SETTLS scheme (Stable Extrapolation Two-Time-Level Scheme, Hortal 2002; Durran and Reinecke 2004) is achieved using other mechanisms.

Gravel et al. did not examine the damping properties of the scheme as revealed in the amplification factor (14.3). In order to examine the damping and its effect on the KE spectra, we first need to estimate the spin-up time for motions as a function their horizontal length scale for comparison with the damping timescale. We can expect that damping in a numerical model will be significant for a particular scale when the decay timescale associated with the damping is of the same order or smaller than the spin-up timescale.

Figure 14.7 show the spin-up time for motions as a function of scale as determined using the turbulence theory of Kolmogorov (1990) and Lindborg's functional fit (Lindborg 1999) for the atmospheric KE spectrum. In essence, the spin-up time scale is an eddy turnover time, and this timescale is given by  $\tau = L(k)/U(k) = [k^3 E(k)]^{-1/2}$ , where  $L$  is the eddy length scale,  $U$  is a velocity scale, and  $E$  is the kinetic energy density. For the energy spectrum depicted in Fig. 14.1, the synoptic scale behaves as  $k^{-3}$  hence the spin-up time asymptotes to a constant value ( $\tau = .68$  days). This estimate of the spin-up time is consistent with the numerical KE analyses of Skamarock (2004) and Hamilton et al. (2008). The spin-up time decreases dramatically as the spectrum transitions to the  $k^{-5/3}$  regime where it behaves as  $k^{-2/3}$ .

<sup>1</sup> Gravel et al. (1993) analyzed the full primitive equations; here we present its simplified form applicable to the shallow water equations.

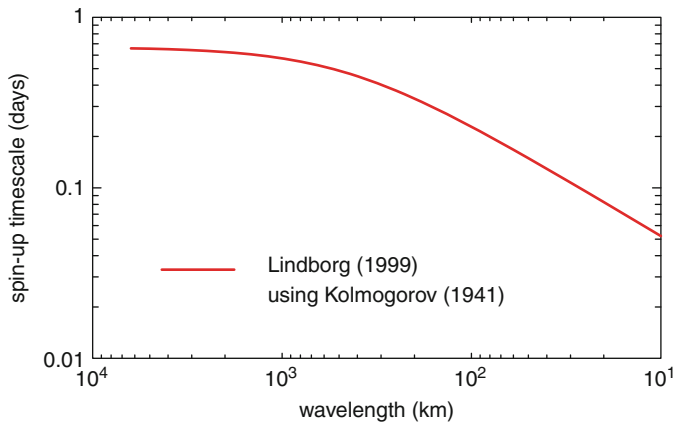
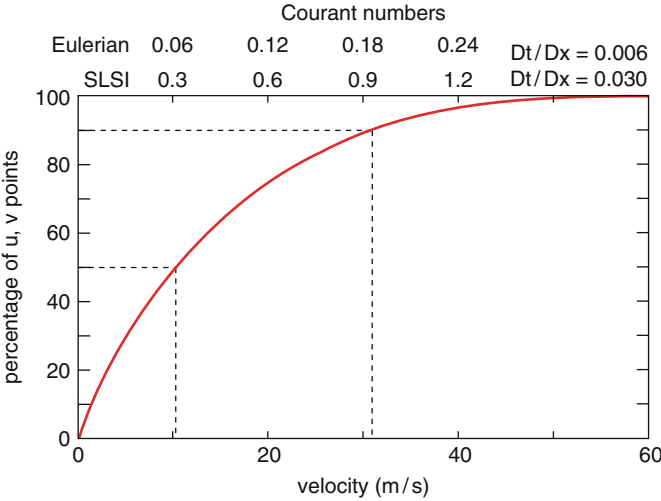


**Fig. 14.7** Spin-up timescale using Kolmogorov's theory (Kolmogorov 1990) and atmospheric spectrum result from Lindborg (1999)

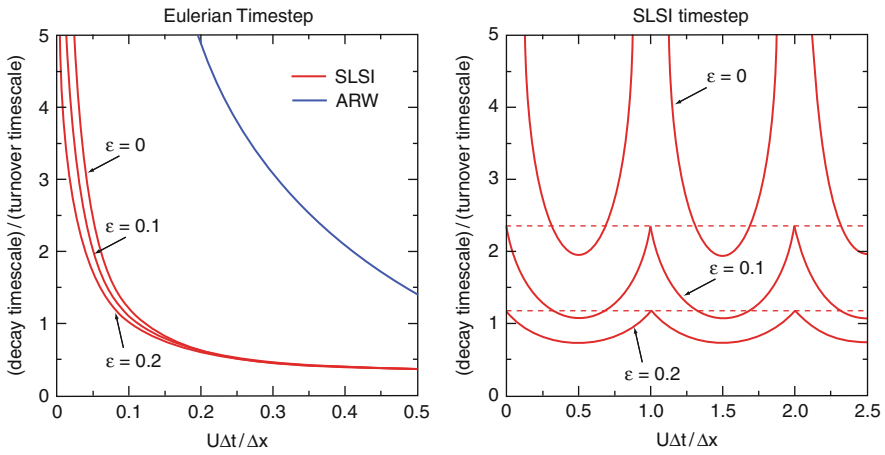
In addition to the spin-up timescale, we need estimates of the Courant numbers typically used the SLSI model applications in order to estimate damping from the transport scheme. Figure 14.8 presents a typical distribution of velocities and Courant numbers for two given values of  $\Delta t / \Delta x$  typically used in Eulerian and semi-Lagrangian models. The Courant number distribution comes from an ARW forecast on a high-resolution grid ( $\Delta x = 5$  km) for the continental US in the winter. For Eulerian timesteps 90% of the Courant numbers on the grid are typically less than 0.2, and only approximately half are less than 0.06. SLSI timesteps are significantly larger than this, and illustrated in the figure is the distribution for an SLSI timestep five times larger than the Eulerian value. For this SLSI timestep 90% of the Courant numbers are less than one, but note that approximately 60% of the Courant numbers are greater than 0.5.

Figure 14.9 presents damping rates normalized by the turnover timescale computed using the amplification factor (14.3) for both Eulerian and SLSI timesteps. We have chosen to examine an  $8\Delta x$  wave which is reasonably well resolved in mesoscale models such as ARW (Skamarock 2004). The damping rates for the SLSI formulation are computed using the cubic interpolation from Gravel et al. (1993), and the computation of the damping rates uses the absolute value of  $E$  from (14.3).

For the Eulerian timestep (the left panel in Fig. 14.9), the damping of the  $8\Delta x$  wave increases dramatically with increasing timestep, and even at a Courant number of 0.05 the decay timescale is only twice the turnover timescale. Most of the Courant numbers will be greater than 0.05 (see Fig. 14.8), hence the damping will be significant. Also notice that the value of the off-centering parameter  $\epsilon$  in (14.3) has little effect on the damping rate which increases slowly with increasing  $\epsilon$ . This behavior indicates that it is the damping from the transport scheme that most affects the waves for the Eulerian timesteps. Also shown in the figure is the damping rate for the ARW model using a fifth order advection scheme. Even though the transport



**Fig. 14.8** Cumulative Courant number distribution for an ARW simulation over the US continent for a 22 January 2005 forecast. Details of the model configuration are given in [Bernardet et al. \(2008\)](#)



**Fig. 14.9** Decay timescale normalized by eddy turnover (spin-up) timescale for a gravity wave with an  $8\Delta x$  wavelength with a horizontal grid-length of 10 km and a timestep of 60 s (Eulerian timestep, *left*) and 300 s (SLSI timestep, *right*). The phase speed of the wave ( $\sqrt{gH}$  in (14.3); in the absence of a mean wind) is 16.667 m/s, hence the Courant number based on this phase speed is 0.1 and 0.5 for the Eulerian and SLSI timesteps, respectively

scheme in this Eulerian model is upwind biased and dissipative, the overall damping is much less than that shown for the SLSI scheme.

For a more typical SLSI timestep (the right panel in Fig. 14.9), the normalized damping appears dramatically different. The damping rates are plotted for three

values of the off-centering parameter  $\epsilon = 0, 0.1$ , and  $0.2$ , and the damping is seen to increase dramatically with increasing  $\epsilon$ . Also apparent is the damping associated with the transport scheme. For integer advective Courant numbers  $U\Delta t/\Delta x$  the semi-Lagrangian transport scheme does not damp, and for non-integer advective Courant numbers the damping is most pronounced half-way between the integer Courant numbers. Operational SLSI weather and climate models must use the off-centering parameter  $0.1 \leq \epsilon \leq 0.2$  for stability in the full nonlinear integrations; hence the damping of the short wavelength high-frequency modes is significant and while there is some damping associated with the semi-Lagrangian interpolation used for transport it does not produce the bulk of the damping for these large timesteps.

These results provide a plausible explanation for the observed behavior of the KE spectrum in SLSI models. Paradoxically, while the damping of the shorter-wavelength high-frequency modes can be attributed to the off-centering of the semi-implicit part of the SLSI formulation when large timesteps are taken, the damping from the interpolations (the response function for the semi-Lagrangian advection,  $\rho$  in (14.3)) dominates when the timestep is reduced to Eulerian values. Reduction of this significant damping likely requires more accurate trajectory integrations that will allow smaller off-centering parameters  $\epsilon$ , but will increase the cost of the integration. The strong damping of the higher-frequency modes also calls into question the efficiency of these schemes for meso- and cloud-scale applications, because, as apparent in the simulated spectra (Shutts 2005) and in this analysis, the long timestep allowable using SLSI formulation comes at a significant cost in accuracy of the small scales. These results are consistent with the theoretical analysis of Bartello and Thomas (1996), who argue that Eulerian timesteps should be used in SLSI schemes at mesoscale resolutions. In addition, Pinty et al. (1995) demonstrate this timestep restriction for accurately simulating vertically propagating gravity waves.

## 14.6 Conclusions

The goal in the design of atmospheric fluid-flow solvers is to maximize efficiency, where efficiency is defined as solution accuracy divided by cost of a given method that attains that accuracy. Given the lack of convergent solutions for turbulent flow, and the acknowledgement that it is the need to resolve previously sub-gridscale structures that drives increasing resolution, an important and relevant measure of accuracy is the ability of a scheme to resolve scales as close to the limit (the smallest scales) as allowable by the discretization. We have shown that examination of a model's KE spectra provides a way to quantify the resolution limits of a model and to determine a model's effective resolution.

Additionally, as global models push into mesoscale and ultimately the cloud-scale, the horizontally divergent modes become the important modes to resolve at the resolution margin, as opposed to the rotational modes for which most large-scale models were designed. The KE spectra reveal these energetics and we have shown

examples where the spectra are used to examine and quantify these regimes and resolution capabilities.

Ultimately, it is the damping characteristics of a model that determine its resolving capabilities. Damping is necessary in atmospheric models because the energy- and enstrophy-cascade dynamics present in the atmosphere demand that there be sinks of energy and enstrophy in the absence of resolved viscous effects. The design of explicit and implicit filters that represent these sinks can impact the effective resolution, but importantly the need for some filters may be dictated by choice of spatial and temporal discretizations, to the detriment of a scheme's resolution capabilities.

For Eulerian discretizations, grid staggering has a significant impact on need for filtering and on the flexibility in filter design and configuration. For example, most mesoscale models use the C-grid staggering which is most accurate for divergent modes. We have shown an example of poor marginal resolution exhibited by the CCSM FV core that uses a D-grid staggering. The FV core needs to use horizontal divergence damping to control grid-scale divergent modes and also uses monotonicity constraints that introduce strong damping into the rotational modes. The effective resolution is only half that of C-grid mesoscale models as revealed in spectra computed from aquaplanet simulations.

Other formulations commonly used in some large scale climate and weather models are also problematic with respect to a scheme's effective resolution. A stability analysis of SLSI schemes that use large timesteps reveals significant damping for high frequency modes because of the need to off-center the semi-implicit time integration in the nonlinear models. The use of Eulerian timesteps in the SLSI models leads to large damping of short wavelengths modes associated with the interpolation scheme in the semi-Lagrangian portion of the algorithm while alleviating the damping associated with the semi-implicit portion of the algorithm.

The SLSI formulations are often stated to be more efficient than Eulerian formulations because the time to solution is less using the SLSI schemes given their comparatively much larger timesteps. However, given their decreased resolution capabilities compared to Eulerian formulations, the SLSI formulations are likely no more efficient and possibly significantly less efficient than Eulerian formulations.

## References

- Arakawa A, Lamb VR (1977) Computational design of the basic dynamical processes of the UCLA general circulation model. *Methods Comput Phys* 17:173–265
- Bartello P, Thomas SJ (1996) The cost-effectiveness of semi-Lagrangian advection. *Mon Wea Rev* 124:2883–2897
- Bernardet L, Nance L, Demirtas M, Koch S, Szoke E, Fowler T, Loughie A, Mahoney JL, Chuang HY, Pyle M, Gall R (2008) The developmental testbed center and its winter forecast experiment. *Bull Amer Meteor Soc* 89:611–627
- Bryan GH, Wyngaard JC, Fritsch JM (2003) Resolution requirements for the simulation of deep moist convection. *Mon Wea Rev* 131:2394–2415
- Collins WD, Rasch PJ, Boville BA, Hack JJ, McCaa JR, Williamson DL, Kiehl JT, Briegleb B (2004) Description of the NCAR Community Atmosphere Model (CAM 3.0). NCAR technical note NCAR/TN464+STR:226 pp.



- Dey CH (1978) Noise suppression in a primitive equations model. *Mon Wea Rev* 106:159–173
- Done J, Davis CA, Weisman ML (2004) The next generation of NWP: Explicit forecasts of convection using the weather research and forecasting model. *Atmos Sci Lett* 5:110–117
- Durran D, Reinecke PA (2004) Instability in a class of explicit two-time-level semi-Lagrangian schemes. *Quart J Roy Meteor Soc* 130:365–369
- ECMWF (2006) Part III: Dynamics and numerical procedures. ECMWF IFS Documentation – Cy31r1 Available at <http://www.ecmwf.int/research/ifsdocs>
- Frisch U (1995) *Turbulence*. Cambridge University Press
- Gravel S, Staniforth A, Côté J (1993) A stability analysis of a family of baroclinic semi-Lagrangian forecast models. *Mon Wea Rev* 121:815–824
- Hamilton K, Takahashi YO, Ohfuchi W (2008) Mesoscale spectrum of atmospheric motions investigated in a very fine resolution global general circulation model. *J Geophys Res* 113
- Hodur R (1997) The Naval Research Laboratory's Coupled Ocean/Atmosphere Mesoscale Prediction System (COAMPS). *Mon Wea Rev* 125:1414–1430
- Hortal M (2002) The development and testing of a new two-time-level semi-Lagrangian scheme (SETTLES) in the ECMWF forecast model. *Quart J Roy Meteor Soc* 128:1671–1687
- Janjic Z (1990) The step-mountain coordinate: Physical package. *Mon Wea Rev* 118:1429–1443
- Janjic Z (2003) A nonhydrostatic model based on a new approach. *Meteor Atmos Phys* 82:271–285
- Kolmogorov A (1990) The local structure of turbulence in incompressible viscous fluid for very large Reynolds number, *dokl. Akad Nauk SSSR* (1941) English translation in *Proc R Soc Lond A* 434 30:9–13
- Lilly D, Bassett G, Droegemeier K, Bartello P (1998) Stratified turbulence in the atmospheric mesoscales. *Theor Comput Fluid Dyn* 11:139–153
- Lin S, Rood RB (1997) An explicit flux-form semi-Lagrangian shallow-water model on the sphere. *Quart J Roy Meteor Soc* 123:2477–2498
- Lindborg E (1999) Can the atmospheric kinetic energy spectrum be explained by two-dimensional turbulence? *Fluid Mech* 388:259–288
- Lindborg E (2006) The energy cascade in a strongly stratified fluid. *J Fluid Mech* 550:207–242
- Lindborg E (2007) Horizontal wavenumber spectra of vertical vorticity and horizontal divergence in the upper troposphere and lower stratosphere. *J Atmos Sci* 64:1017–1025
- Lindborg E, Berthouwer G (2007) Stratified turbulence forced on rotational and divergent modes. *J Fluid Mech* 586:83–108
- Lindborg E, Cho JY (2000) Horizontal velocity structure functions in the upper troposphere and lower stratosphere. 2 Theoretical considerations *J Geophys Res* D10, 11 106:0233–1024
- Mason P (1994) Large-eddy simulation: A critical review of the technique. *Quart J Roy Meteor Soc* 120:1–26
- Nastrom G, Gage KS (1985) A climatology of atmospheric wavenumber spectra of wind and temperature observed by commercial aircraft. *J Atmos Sci* 42:950–960
- Pinty JP, Benoit R, Richard E, Laprise R (1995) Simple tests of a semi-implicit semi-Lagrangian model on 2d mountain wave problems. *Mon Wea Rev* 123:3042–3058
- Randall D (1994) Geostrophic adjustment and the finite difference shallow-water equations. *Mon Wea Rev* 122:1371–1377
- Shutts G (2005) A kinetic energy backscatter algorithm for use in ensemble prediction systems. *Q J Roy Meteor Soc* 131:3079–3102
- Skamarock W (2004) Evaluating mesoscale NWP models using kinetic energy spectra. *Mon Wea Rev* 132:3019–3032
- Skamarock WC, Klemp JB (2008) A time-split nonhydrostatic atmospheric model for weather research and forecasting applications. *J Comput Phys* 227(7):3465–3485
- Skamarock WC, Klemp JB, Dudhia J, Gill DO, Barker DM, Duda MG, Huang XY, Wang W, Powers JG (2008) A description of the Advanced Research WRF version 3. *Ncar Technical Journal NCAR/TN-475+STR*, 113 pp
- Staniforth A, Wood N (2008) Aspects of the dynamical core of a nonhydrostatic, deep-atmosphere, unified weather and climate-prediction model. *J Comput Phys* 227(7):3445–3464

- Takahashi YO, Hamilton K, Ohfuchi W (2006) Explicit global simulation of the mesoscale spectrum of atmospheric motions. *Geophys Res Lett* 33:L12,812
- Tao WK, Moncrieff MW (2009) Multiscale cloud system modeling. *Rev Geophys* 47: 41pp
- Weisman ML, Skamarock WC, Klemp JB (1997) The resolution dependence of explicitly modeled convective systems. *Mon Wea Rev* 125:527–548
- Wyngaard JC (2004) Changing the face of small-scale meteorology. In: Federovich, Rotunno, Stevens (eds) *Atmospheric Turbulence and Mesoscale Meteorology*, Cambridge University Press, pp 17–34
- Xue M, Droegemeier KK, Wong V (1990) The advanced regional prediction system (ARPS) - a multiscale nonhydrostatic atmospheric simulation and prediction tool. Part I Model dynamics and verification *Meteor Atmos Phys* 75:339–356
- Yeh KS, Côté J, Gravel S, Méthot A, Patoine A, Roch M, Staniforth A (2002) The CMC-MRB Global Environmental Multiscale (GEM) model. Part III: Nonhydrostatic formulation. *Mon Wea Rev* 130:339–356